Paper presented at the 25th International Society of Air-breathing Engines Conference (ISABE 2022). Ottawa, Canada, September 25-30, 2022

Effect of nozzle chevron technology on the near-field contrail properties behind an aircraft engine using a CFD-microphysics coupling

Sébastien Cantin, Adrien Misandeau, Mohamed Chouak, and François Garnier
sebastien.cantin.1@ens.etsmtl.ca
École de Technologie Supérieure
Mechanical Engineering Department
University of Quebec
Montreal, QC
Canada

ABSTRACT

The formation of ice-particles in near-field aircraft plumes at cruise altitudes generates contrails. The latter trigger the formation of large cirrus clouds, called aircraft-induced clouds (AICs). These artificial clouds result in a net positive radiative forcing (warming) effect. Furthermore, the use of chevrons in modern jet engines helped to reduce jet noise of 'separate-flow' nozzles; however, the impact of this technology on near-field contrail properties has not been investigated. In this context, this paper presents a CFD-microphysics coupling strategy to model the 3-D dynamics and microphysical transformations in the near-field plume of an aircraft engine. The study investigates the effect of implementing the chevron technology in both fan and core nozzles on plume and ice-particle properties. For this purpose, 3-D unsteady Reynolds-Averaged Navier-Stokes simulations were carried out behind a realistic LEAP-1A engine geometry (high bypass-ratio 10.5:1) at cruise conditions. The microphysical modeling accounts for the main process of water-vapor condensation on pre-activated soot particles known as heterogeneous condensation. The plume dilution and ice crystals formation in the engine near-field jet were validated using available numerical and in-flight data to demonstrate the predictive capabilities of the proposed modeling strategy. Different geometrical parameters of fan- and core-nozzles were investigated by varying the number and the penetration angle of chevrons. The comprehensive analysis showed that core-chevron nozzles lead to higher kinetic turbulent energy, higher liquid saturation ratio, larger ice particles and thicker contrails than chevron fan-nozzles and the baseline nozzle without chevrons. The proposed model can be hence used in future studies to characterize the impact of tabs or lobed nozzle-exit parameters on the optical and microphysical properties of near-field contrails.

Keywords: Aircraft engine emissions, Contrails, Near-field plume properties, CFD, Microphysics coupling, Eulerian-Lagrangian approach, Ice particle formation, Chevron technology.

NOMENCLATURE

AIC	Aircraft Induced Cirrus
GCI	Grid Convergence Index
GMD	Geometric Mean Diameter
LES	Large Eddy Simulation
TKE	Turbulent Kinetic Energy
URANS	Unsteady Reynolds Average Navier-Stokes

Symbols

θ_c	Chevron penetration angle
λ_l	Wavelength to visible light
μ_r	Refractive index for ice
ρ	Density
τ_v	Optical depth
Φ_c	Chevron half-angle
ω_{ice}	Ice mass sink term
A	Kelvin effect term
C_{BC}	Black Carbon concentration
D_b	Bypass diameter
EI_{iceno}	Ice number emission index
EI_m	Mass emission index
EI_n	Number emission index
L	Domain length
M	Mach number
N	Dilution ratio
N_c	Number of chevrons
N_{com}	Number of computational particles
N_p	Number of physical particles
p	Pressure
P_w	Water vapour partial pressure
$P^0_{w,ice}$	Ice saturated vapour pressure
$P^0_{w,liq}$	Liquid saturated vapour pressure
Q_{ext}	Mie extinction efficiency
R	Domain radius
r_p	Particle radius
r_b	Bypass radius
S_{ice}	Ice saturation ratio
S_{liq}	Liquid saturation ratio
SN	Smoke Number
T	Temperature
U	Velocity
V	Cell volume
X	Mole fraction
Y	Mass fraction
Z	Passive scalar

Subscripts

a	Air
b	Bypass
c	Core
g	Gas
p	Particle
w	Water vapour

1.0 INTRODUCTION

Overall, aviation's contribution to anthropogenic climate change is estimated to be about 5%, of which approximately 66% can be attributed to the non-CO_2 effects [1]. One of the major contributor to aviation's non-CO_2 effects is related to water vapour emissions that trigger the formation of contrails behind aircraft engines. Consistent jet contrails evolve to contrail cirrus that increase the cloud coverage. By reflecting in/outgoing radiation, aircraft-induced clouds (AICs) result in a positive radiative forcing (warming) effect [2]. In this regard, altering contrails at the formation stage is considered to be a promising means to help reduce the aviation's impact on the global radiation budget of the earth [3].

Contrails are line-shaped clouds that are typically formed in the first second(s) of plume mixing. These clouds are made of ice particles that mainly form by the heterogeneous condensation of water vapour onto activated soot particles behind aircraft engine. Observation data in literature indicate that the number of ice particles is directly governed by the engine-exhaust conditions and remains relatively constant during the lifetime of contrails [4]. Therefore, it is important to study the contrail formation to 1) provide the microphysical and dynamic properties necessary for the assessment of contrails' radiative forcing over their whole lifetime, and to 2) investigate new engine technologies aiming at reducing non-CO_2 emissions directly at the source, thereby minimizing their environmental impact.

With the recent advances in computational resources, numerical investigations have attracted increasing interest in better characterizing contrail-dependent factors. In this regard, the early stage of contrail formation is particularly interesting as most of the controlling factors can be traced directly back to engine or aircraft characteristics such as the soot emission index EI_{soot}, the propulsion efficiency or the bypass ratio. Modeling formation of near-field contrails behind aircraft engine involve complex phenomena such as turbulent mixing, compressibility effects, chemical transformations, and microphysics. To simulate these phenomena, several modeling approaches for near-field models have used in the literature. For instance, Kärcher et al. [5] used 0-D microphysical models and found that the number of ice particles scales roughly in proportion the number of emitted soot particles (condensation nuclei). This type of model however showed some discrepancies as compared to in-flight measurements due to (1) the absence of a detailed turbulence modeling, and (2) the simplified level of dynamics using averaged bulk exhaust (provided by semi-empirical models). Some authors remedied the shortcomings through offline-coupling strategies with an external fluid-flow solver (offline approach) [6]. Over the last two decades, computational cost effectiveness has increased interest in 3D CFD-based models to refine the early plume dynamics and associated mixing process. For example, Paoli et al. [7] used large eddy simulations (LES) for modeling free turbulent jets with classical law expansion to investigate contrail formation for two- and four-engine configurations. These simplified representations of the nozzle exhaust jet neglect the nozzle exit-related aspects. Lewellen [8] used 3D LES with a binned resolved microphysics approach to model the evolution of soot, ambient and volatile particles. LES initialization of the jet was made using 2D RANS fields one meter downstream from the engine exit plane of a single uninstalled engine of a B737 aircraft. Khou et al. [9] investigated with a RANS approach the near-field contrail behind a realistic twin-jet Boeing 737 geometry using simplified coplanar exits for both fan and core nozzle flows. Although their model accounts for an advanced microphysics of both soot and ice particles with a tabulated-chemistry of gaseous fuel-combustion products, nozzle features like chevrons that might impact the near-field mixing [10], thereby the ice-particle formation, were not considered. In modern jet engines, the chevron technology is used to create stream-wise vorticity that has an impact on the mixing of the jet and generally reduces the low frequency noise of the spectrum of 'separate-flow' nozzles [11, 12]. However, the impact of this technology on near-field contrail properties remain unclear.

Therefore, the objective of the present paper is to investigate the effect of engine chevron nozzles on the near-field properties of contrails using a URANS CFD-microphysics coupling. To the authors' knowledge, no contrail study has investigated the effect of chevron nozzles. As such, different geometrical parameters of fan- and core-exit

nozzles are hence investigated by varying the chevron number and penetration angle [13] of the LEAP-1A core- and bypass-nozzles. The modeling capabilities of the near-field contrail model presented in our previous work [14] are extended here by updating the microphysical model (calculation of saturation pressure, evaporation) for ice crystals.

2.0 MODEL DESCRIPTION

2.1 Modeling approach of near-field contrail formation

The modeling approach for the formation of ice particles is schematically represented in Figure 1. The nozzle exit flow from a turbofan engine at cruise flight consists of two jets: a core (hot) flow and a surrounding bypass (cold) flow. Both jets are mixed with the freestream moist air. The bypass flow contains ambient moist air that has been slightly accelerated by the engine fan, while the core jet drives the fuel-combustion products composed of gaseous emissions laden with soot particles (solid phase). Water vapour in the dilution plume condenses onto soot particles, which serve as condensation nuclei when activated with sulfuric acid (heterogeneous nucleation [15, 16]). Under saturation conditions, ice particles form and grow by taking up more condensable matter, i.e. water vapour, from the plume and ambient air, leading to contrail formation.

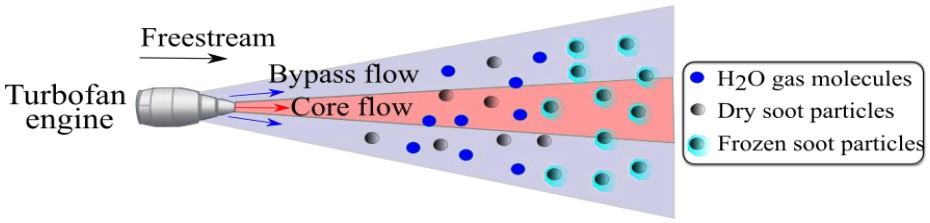

Figure 1: 2D Scheme of the exhaust jet from a turbofan engine with ice-particles and aerosol formation

In this study, the Eulerian-Lagrangian approach was used to model the formation of contrail ice particles in the LEAP-1A engine near field. The continuous gas phase was modeled with the Eulerian approach, while the dispersed-phase of solid particles (soot and ice particles) were tracked with the Lagrangian approach. Lastly, a one-way microphysical coupling was considered to account for ice particle growth due to water vapour condensation.

2.2 Gas-phase equations

The compressible flow of the gas phase ('g' index) is considered to be a mixture of two miscible species: air ('a' index) and water vapour ('w' index). Assuming an ideal gas, the mixture density $\overline{\rho}_g$, temperature $\tilde{T}_g$, and pressure $\overline{p}_g$ are linked with the equation of state

$$\overline{p}_g = \overline{\rho}_g r_g \tilde{T}_g \tag{1}$$

where r_g is the specific gas constant. The overbar sign $-$ denotes the Reynolds (or ensemble) averaging, while $\sim$ refers to the Favre (or density-weighted) averaging defined as $\bar{\rho}\tilde{\Phi} = \overline{\rho\Phi}$ and $\Phi = \tilde{\Phi} + \Phi''$ which accounts for compressibility effects. As the growth of ice particles is a time-dependent process, the flow is assumed to be unsteady. Therefore, the unsteady Favre-averaged Navier–Stokes (FANS) equations expressing the conservation of the gas-phase global mass, momentum, and energy were solved. In Cartesian coordinates ($\boldsymbol{i}$, $\boldsymbol{j}$, $\boldsymbol{k}$), these equations read as follow with some modeling assumptions [17]

$$\frac{\partial \overline{\rho}_g}{\partial t} + \frac{\partial}{\partial x_i}\left(\overline{\rho}_g \tilde{u}_{i,g}\right) = 0 \tag{2}$$

$$\frac{\partial}{\partial t}\left(\overline{\rho}_g \tilde{u}_{i,g}\right) + \frac{\partial}{\partial x_j}\left(\overline{\rho}_g \tilde{u}_{i,g}\tilde{u}_{j,g}\right) = \frac{\partial}{\partial x_j}\left(-\overline{P}_g\delta_{ij} + \widetilde{\tau}_{ij}^{visc} + \widetilde{\tau}_{ij}^{turb}\right) \tag{3}$$

$$\begin{aligned}\frac{\partial}{\partial t}\left(\overline{\rho}_g \tilde{e}_g^{tot}\right) + \frac{\partial}{\partial x_j}\left(\overline{\rho}_g \tilde{u}_{j,g}\tilde{e}_g^{tot} + \tilde{u}_{j,g}\overline{p}_g\right) \\ = \frac{\partial}{\partial x_j}\left(\tilde{q}_{j,g}^{visc} + \tilde{q}_{j,g}^{turb}\right) - \frac{\partial}{\partial x_j}\left(\tilde{u}_{i,g}\left(\widetilde{\tau}_{ij}^{visc} + \widetilde{\tau}_{ij}^{turb}\right)\right)\end{aligned} \tag{4}$$

Solving Eqns. (2)-(4) provides the primary variables of the mean flow $\overline{\rho}_g$, the velocity field $\tilde{\boldsymbol{u}}_g = \left(\tilde{u}_g, \tilde{v}_g, \tilde{w}_g\right)$, and the total energy $\tilde{e}_g^{tot}$, such as $c_{p,g}$ denotes the specific heat μ_g the dynamic viscosity, $\mu_{t,g}$ the eddy viscosity, Pr_g the Prandtl number, and $Pr_{t,g}$ the turbulent Reynolds number of the gas phase. The latter physical properties are all functions of $\tilde{T}_g$, which was derived from the total energy using Eq. (5). The averaging of nonlinear terms on the right-hand side of Eqns. (3) and (4) yields the Reynolds stress $\widetilde{\tau}_{ij}^{turb}$ and the turbulent heat flux $\tilde{q}_{j,g}^{turb}$, in addition to their laminar (or viscous) counterparts $\widetilde{\tau}_{ij}^{visc}$.and $\tilde{q}_{j,g}^{visc}$, given by Eqns. (6)−(9), respectively, for a Newtonian fluid.

$$\tilde{e}_g^{tot} = c_{v,g}\tilde{T}_g + \frac{\tilde{u}_{k,g}\tilde{u}_{k,g}}{2} + \frac{\widetilde{u_{k,g}''u_{k,g}''}}{2} \tag{5}$$

$$\widetilde{\tau}_{ij}^{visc} = \mu\left(\frac{\partial \tilde{u}_{i,g}}{\partial x_j} + \frac{\partial \tilde{u}_{j,g}}{\partial x_i} - \frac{2}{3}\frac{\partial \tilde{u}_{k,g}}{\partial x_k}\delta_{ij}\right) \tag{6}$$

$$\begin{aligned}\tau_{ij}^{turb} &= -\overline{\rho_g u_{i,g}'' u_{j,g}''} \\ &= \mu_{t,g}\left(\frac{\partial \tilde{u}_{i,g}}{\partial x_j} + \frac{\partial \tilde{u}_{j,g}}{\partial x_i} - \frac{2}{3}\frac{\partial \tilde{u}_{k,g}}{\partial x_k}\delta_{ij}\right) - \frac{1}{3}\overline{\rho}_g\widetilde{u_{k,g}''u_{k,g}''}\delta_{ij}\end{aligned} \tag{7}$$

$$\tilde{q}_{j,g}^{visc} = c_{p,g}\frac{\mu_g}{Pr_g}\frac{\partial \tilde{T}_g}{\partial x_j} \tag{8}$$

$$\tilde{q}_{j,g}^{turb} = c_{p,g}\frac{\mu_{t,g}}{Pr_{t,g}}\frac{\partial \tilde{T}_g}{\partial x_j} \tag{9}$$

To compute the mixture composition in the gas phase ($\Phi_{\mathrm{g}} = \tilde{Y}_a\Phi_{\mathrm{a}} + \tilde{Y}_w\Phi_{\mathrm{w}}$), the mass fractions of air and water vapour ($\tilde{Y}_a$ and $\tilde{Y}_w$, respectively) are derived using Eqns. (10) and (11).

$$\frac{\partial}{\partial \mathrm{t}}\left(\bar{\rho}_g\tilde{Y}_w\right) + \frac{\partial}{\partial x_i}\left(\bar{\rho}_g\tilde{Y}_w\tilde{u}_{i,g}\right) - \frac{\partial}{\partial x_i}\left(\left(\frac{\mu_g}{\sigma_g} + \frac{\mu_{t,g}}{\sigma_{t,g}}\right)\frac{\partial \tilde{Y}_w}{\partial x_i}\right) = -\overline{\omega}_{\mathrm{ice}} \tag{10}$$

$$\tilde{Y}_a = 1 - \tilde{Y}_w \tag{11}$$

Equation (10) translates the mass conservation of water vapour where the source term $\overline{\omega}_{\mathrm{ice}}$ on the right-hand side is the rate of condensed matter representing the mass transfer due to ice-particle growth. This coupling term is presented in greater detail in the next section. The variables σ_g and $\sigma_{t,g}$ denote the Schmidt number and the turbulent Schmidt number, respectively taken as being equal to 1 [18] and 0.9 [9, 19].

2.3 Turbulence model

To close the set of gas-phase equations, the eddy viscosity $\mu_{t,g}$ term introduced by the Boussinesq approximation (Eq. (7)) was modeled using the Realizable $k-\varepsilon$ model [20] to close the set of equations. This model is known to provide improved predictions in terms of the dissipation rate for round jets [21]. It was chosen based on validation results performed in a previous work [14] after comparing three eddy-viscosity models to the available experimental data in the case of compressible coaxial jets. The $k-\varepsilon$ Realizable formulation uses two transport equations: one for the turbulent kinetic energy k and one for the dissipation rate ε, such as

$$S_{ij} = \frac{1}{2}\left(\frac{\partial \tilde{u}_{i,g}}{\partial x_j} + \frac{\partial \tilde{u}_{j,g}}{\partial x_i}\right) \tag{12}$$

$$\mu_{t,g} = \bar{\rho}_g C_\mu \frac{k^2}{\varepsilon} \tag{13}$$

$$\frac{\partial}{\partial \mathrm{t}}\left(\bar{\rho}_g k\right) + \frac{\partial}{\partial x_i}\left(\bar{\rho}_g k \tilde{u}_{i,g}\right) = -\frac{\partial}{\partial x_i}\left(\frac{\mu_{t,g}}{\sigma_k}\frac{\partial k}{\partial x_i}\right) + 2\mu_{t,g} S_{ij} \cdot S_{ij} - \bar{\rho}_g \varepsilon \tag{14}$$

$$\frac{\partial}{\partial t}\left(\bar{\rho}_g \varepsilon\right) + \frac{\partial}{\partial x_i}\left(\bar{\rho}_g \varepsilon \tilde{u}_{i,g}\right) = \frac{\partial}{\partial x_i}\left(\frac{\mu_{t,g}}{\sigma_\varepsilon}\frac{\partial \varepsilon}{\partial x_i}\right) + 2C_{1\varepsilon}\mu_{t,g}\frac{\varepsilon}{k} S_{ij} \cdot S_{ij} - C_{2\varepsilon}\bar{\rho}_g \frac{\varepsilon^2}{k + \sqrt{\nu_g \varepsilon}} \tag{15}$$

where $S_{ij} = \frac{1}{2}\left(\partial \tilde{u}_{i,g}/\partial x_j + \partial \tilde{u}_{j,g}/\partial x_i\right)$ represents the deformation rate of the mean flow, while C_μ, σ_k, σ_ε, $C_{1\varepsilon}$, and $C_{2\varepsilon}$ are the model constants (see [22]).

2.4 Dispersed-phase flow

At cruise conditions, the number density of physical particles is so high that a modeling simplification is required to save the simulation time. For example, a typical value for emitted soot particles from an engine nozzle is about 10 #/m3 [23]. Therefore, computational particles are considered as spheres of radius r_p, with each representing N physical particles [24]. Numerically, soot and ice particles are treated as passive tracers since their size and relaxation time are relatively small as compared to the characteristic scales of the gas-phase flow (for ice particles $\tau_p \sim 10^{-5}$ s with the largest r_p about few microns) [25]. Thus, they have the same velocity as the carrier phase, but the drag and gravity forces are neglected since they have neither mass nor volume. The equation governing particle movement reads as follows

$$\frac{d\boldsymbol{x}_p}{dt} = \tilde{\boldsymbol{u}}(\boldsymbol{x}_p, \mathrm{t}) \tag{16}$$

where $\boldsymbol{x}_p$ is the particle position vector.

2.5 Ice-particle microphysics

In jet contrails, ice-particle growth is due to condensation of water vapour onto suitable nucleation sites or pre-activate particles (mostly soot particles) [26]. The ratio between the local water vapour partial pressure (P_w) and the saturated vapour pressures ($P^0_{w,liq}$ and $P^0_{w,ice}$) defines the saturation ratios with respect to liquid water noted S_{liq} and with respect to ice noted S_{ice} [27]

$$S_{liq} = \frac{P_w\left(\tilde{T}_p\right)}{P^0_{w,liq}\left(\tilde{T}_p\right)} \tag{17}$$

$$S_{ice} = \frac{P_w\left(\tilde{T}_p\right)}{P^0_{w,ice}\left(\tilde{T}_p\right)} \tag{18}$$

such as the local partial pressure P_w is calculated according to Dalton's law:

$$P_w\left(\tilde{T}_p\right) = \mathrm{X}_w P_{tot} \tag{19}$$

where X_w is the mole fraction of water vapour and P_{tot} is the absolute total pressure. The saturated vapour pressures with respect to liquid water $\left(P^0_{w,liq}\right)$ and with respect to ice $\left(P^0_{w,ice}\right)$ are calculated according to Murphy and Koop [28]

$$P_{w,liq}^{0}(\tilde{T}_p) = \exp\Bigg(54.842763 - \frac{6763.22}{\tilde{T}_p} - 4.21 \cdot \ln(\tilde{T}_p) + 0.000367 \cdot \tilde{T}_p + \tanh\Big(0.0415 \cdot (\tilde{T}_p - 218.8)\Big)\Big(53.878 - \frac{1331.22}{\tilde{T}_p} - 9.44523 \cdot \ln(\tilde{T}_p) + 0.014025 \cdot \tilde{T}_p\Big)\Bigg) \tag{20}$$

$$P_{w,ice}^{0}(\tilde{T}_p) = \exp\left(9.550426 - \frac{5723.265}{\tilde{T}_p} + 3.53068 \cdot \ln(\tilde{T}_p) - 0.00728332 \cdot \tilde{T}_p\right) \tag{21}$$

Both saturation ratios S_{ice} and S_{liq} increase with the plume dilution in the exhaust jet, such as $S_{ice} > S_{liq}$. At first, the condensation of liquid water on initially activated soot particles (i.e. heterogeneous nucleation) is triggered when $S_{liq} = 1$. Then, the growth of spherical-shaped ice particles continues in the dilution plume up to the point where $S_{ice} = 1$. Beyond this point ($S_{ice} \leq 1$), further dilution of the exhaust plume causes the sublimation of ice particles so as to restore water vapour to the ambient air. In this study, the microphysics of ice-crystal growth was modeled, while the processes of soot activation [29] and homogeneous ice nucleation [30] were not taken into account. Therefore, the transition from continuum to molecular regime is supposed as being instantaneous [31]. The mass and size change of a single particle due to condensation/sublimation effects can be expressed by a diffusion law as described by the model of Fukuta and Walter [31]

$$\dot{m}_p = \frac{dm_p}{dt} = \frac{4\pi\rho_p r_p\,(S_{liq} - A)}{C_T A + C_\rho} \tag{22}$$

$$\dot{r}_p = \frac{dr_p}{dt} = \frac{S_{liq} - A}{r_p(C_T A + C_\rho)} \tag{23}$$

where m_p denotes the mass of a particle p, ρ_p its density, and A the Kelvin effect. The latter is calculated from

$$A = \exp\left(\frac{2\sigma M_w}{r_p \rho_p r_g \tilde{T}_g}\right) \tag{24}$$

where σ denotes the surface tension of water. The factors C_T and C_ρ in equations (22) and (23) control the water vapour temperature and air density just above the particle surface. The detailed formulations of both factors can be found in [14]. Therefore, we obtain the mass variation of each ice crystal and a fortiori the vapour mass variation. This leads to the coupling term $\overline{\omega}_{\text{ice}}$ in Eq. (10), which can be derived as follows

$$\overline{\omega}_{\text{ice}} = n \sum_{p=1}^{N_{com}} \dot{m}_p \tag{25}$$

where n is the number density of particles contained in a volume cell V, such that $n = N_p/V$. The total number of computational particles is N_{com}, each of them representing N_p physical particles. More details about the model are available in Fukuta and Walter [31]. The latter model was implemented in a microphysical module and coupled to the CFD commercial code in Simcenter Star-CCM+ v16.06. A detailed description of the numerical strategy is provided below.

3.0 COMPUTATIONAL SETUP

3.1 CFD domain

The 3D CAD of the short-cowl nozzle is representative of the LEAP-1A35A engine [32] (see Figure 3-c), in which a central plug is included to encourage early mixing between the core and bypass flows. The engine geometry is composed of a core and a bypass flow whose diameters are $D_c = r_c/2 = 0.942\ m$ and $D_b = r_b/2 = 1.864\ m$, respectively. The internal ducts of both bypass and core jets were modelled in order to allow for the development of the jet boundary layers. As the realistic engine LEAP-1A35A includes chevrons nozzle on the outer nozzle diameter of the bypass, 3D rounded chevrons are generated. As shown in Figure 3-a, a 90° sector based on the engine nozzle was considered for the URANS calculations assuming that the mean flow is axisymmetric. The computational domain (Figure 3-b) has a radius $R = 5D_b$ and a length $L = 76D_b$ to ensure ambient pressure as a far-field boundary condition.

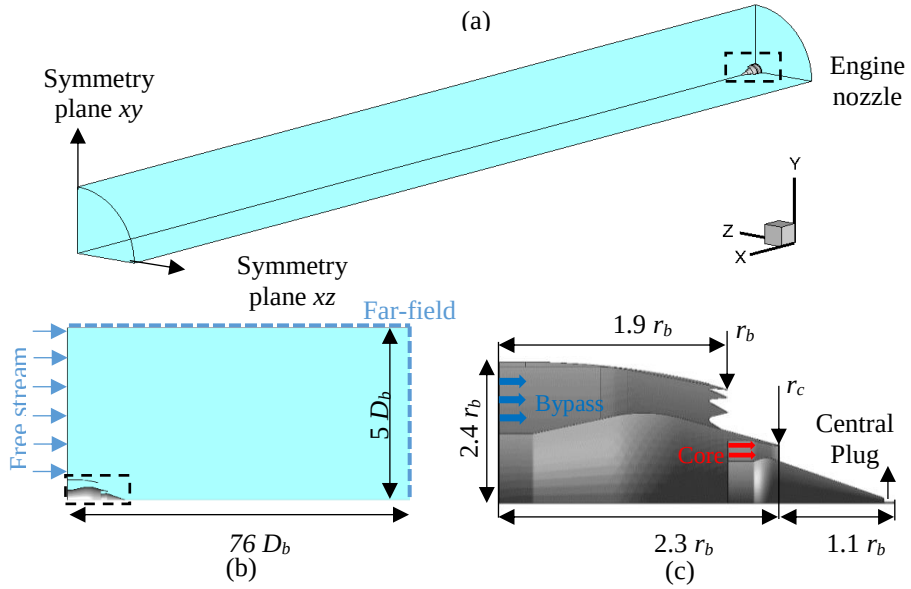

Figure 2: Computational domain and boundary conditions for the LEAP-1A35A: (a) isometric view, (b) 2D lateral view, (c) nozzle exhaust geometry

3.2 Nozzle configurations

To study the effect of chevron nozzles on jet contrail formation, a total of eight configurations were investigated as summarized in Table 1: baseline configuration without chevrons (BB), chevron bypass-nozzles (BC12, BC16, BC24), chevron core-nozzles with 0° penetration angle (C12B, C16B, C24B), and with 5° penetration angle (C12BP5). Figure 3 presents the geometric parameters of chevron nozzles presented in Table 1, namely the chevron half-angle Φ_c, the arc length at chevron base L_a, the chevron number N_c, and the chevron penetration angle θ_c expressing the angle between the chevron tip and base radii. For all configurations, the chevron length along the flow path L_c is taken equal to $0.1D_b$, while the number of chevrons and the penetration angle were modified following noise and dynamic studies [33-35] to investigate here their effects on microphysical properties of associated jet contrails.

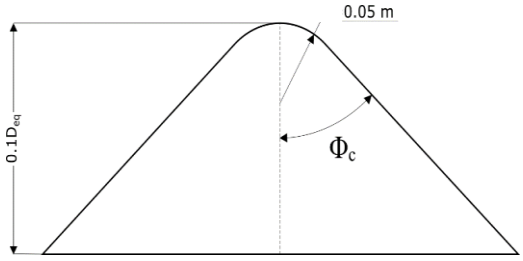

Figure 3: 2D Schematic of rounded chevrons

Table 1: Summary of the studied nozzle configurations and parameters

	Configuration	Number of chevrons N_c	Chevron half-angle Φ_c (deg)	Penetration angle θ_c (deg)
Baseline nozzle	BB	0	-	-
Chevron fan-nozzles	BC12	12	57.3	0
	BC16	16	48.1	0
	BC24	24	32.5	0
Chevron core-nozzles	C12B	12	30	0
	C16B	16	30	0
	C24B	24	30	0
	C12BP5	12	30	5

3.3 Aerothermodynamic boundary conditions

Three inlet sections were used upstream: a freestream inlet (M_{amb}^0, T_{amb}^0) as shown in Figure 3-b, a bypass pressure inlet (P_b, T_b), and a core pressure inlet (P_c, T_c) as shown in Figure 3-c. A no-slip adiabatic condition was imposed on engine walls, while a symmetry condition was used on both lateral planes (see Figure 3-a). Remaining boundaries were treated with an ambient pressure far-field condition (Figure 3-b). The software GasTurb was used to determine the aerothermodynamic parameters (temperature, pressure, and velocity) across the different engine stages. A generic two-spool, unmixed-flow, turbofan engine configuration was chosen to model the LEAP-1A35A engine at cruise flight conditions. The engine design parameters, such as the rated thrust, bypass ratio, and the overall pressure ratio, were gathered from the International Civil Aviation Organization (ICAO) Emission Databank [36] and the European Aviation Safety Agency (EASA) type-certificate data sheet [37]. The engine-exit parameters from the GasTurb model were used as inlet conditions for both core and bypass jets in the CFD simulations (see Table 2).

Ice-particle formation was modelled in the exhaust plume of the LEAP-1A35A engine at realistic cruise flight conditions at 35,000 feet and a Mach number $M_{amb}^0 = 0.8$. The ambient static temperature and pressure values were $T_{amb} = 219\,\text{K}$ and $P_{amb} = 23{,}800\,\text{Pa}$, respectively. The molar fraction of water vapour was set at $Y_{amb} = 6.08 \times 10^{-5}$ to account for 60% of relative humidity. The initial water molar fraction in the core jet was set at 2.2×10^{-2} [38]. A turbulence intensity of 10% was used for both exhaust jets, while a value of 0.1% was applied on freestream and far-field boundary conditions, as per Garnier, Baudoin [39].

Table 2: LEAP-1A35A exhaust properties at cruise flight conditions

	Parameters	Settings
Core flow	Mach, M_c	0.37
	Velocity, U_c (m.s^{-1})	182.8
	Static temperature, T_c (K)	624.6
	Number emission index, EI_n (#/kg-fuel)	9.79×10^{13}
	Mass emission index, EI_m (kg/kg-fuel)	4.13×10^{-3}
	Number density of soot particles, n (#.m^{-3})	4.35×10^{11}
	Number of computational particles, N_{com} (#)	6086
	Geometric mean diameter, GMD (nm)	11.64
	Soot-particle distribution	Monodisperse
	Molar fraction of water vapour, Y_c	2.2×10^{-2}
Bypass flow	Mach, M_b	0.478
	Velocity, U_b (m.s^{-1})	156.7
	Static temperature, T_b (K)	267

3.4 Soot particle initialization

Table 2 summarizes the soot particles properties considered at the LEAP-1A35A core exhaust. A monodisperse soot particle distribution was considered, i.e. all emitted particles are treated as spheres having the same radius r_p, as per [6, 8]. To estimate mean exhaust properties at cruise flight conditions (~20% of the maximum rated thrust [38]), emission indices of soot particles in number and mass, respectively EI_n (#/kg-fuel) and EI_m (mg/kg-fuel), were computed using the manufacturer's proprietary correlations and the known emission properties from the ICAO Emission Databank at the equivalent ground power setting of 20% (by interpolation of the LTO-cycle data). Since the geometric mean diameter (GMD) of soot particles is not available in the ICAO Emission Databank, the experimental correlation developed by Agarwal, Speth [39] was used to estimate the engine exit-plane GMD

$$\mathrm{GMD} = a(C_{BC})^b \tag{26}$$

such as a and b are constants equal to 5.08 nm and 0.185. The black carbon concentration C_{BC} is computed as follows [39]

$$C_{BC} = \frac{648.4\ e^{0.0766\times SN}}{1 + e^{-1.098(SN-3.064)}} \tag{27}$$

where the value of smoke number (SN) is 1.284 at the ground power setting of 20% (cruise-equivalent power setting). The latter value was interpolated from the ICAO LTO-cycle emission databank [36]. Due to the relatively high number density of soot particles ($n = 4.35 \times 10^{11}$ #.m^{-3}), the simulation cost was alleviated by considering numerical particles instead of physical particles, such as each numerical particle represents the motion of N_p physical particles. Numerical particles. According to Paoli et al. [7], a number of physical soot particles in the range $10^6 - 10^8$ preserves the statistical reliability of the simulation results. As such, a number $N_p = 8.8 \times 10^6$ of physical particles was used herein, thus 6,086 numerical particles were injected from the core inlet boundary at each time step and tracked in the computational domain during the simulation time.

3.5 Mesh and discretization schemes

The mesh of the computational domain is made of a structured Cartesian block mainly composed of cubic cells ($\Delta x = \Delta y = \Delta z$) as illustrated in Figure 4 for medium grid. The latter was chosen based on a grid convergence study performed using three grids for the BB and BC24 configurations (see Table 1): coarse (3.3M and 3.7M cells), medium (9.5M and 10.7M cells), and fine (26.2M and 29.2M cells), labeled hereafter grid '3', '2', and '1', respectively. The discretization errors were estimated using the GCI method [40] on a probe located in the mixing shear layer between the core and the bypass jets (i.e. probe placed at $x = 0.16D_b, y = -z = 0.2D_b$).Three flow variables were used to compute the discretization errors: static temperature, water vapour molar fraction, and core axial velocity. GCI results summarized in Table 3 showed that the discretization errors are sufficiently low (below 1%) for all studied grids and using the three flow variables. The highest GCI errors (about 0.6%) were computed between coarse and medium grids for the water vapour molar fraction.

Table 3: Mean relative error ε, standard deviation σ, and GCI results in the mixing shear layer (probe at $x = 0.16D_b, y = -z = 0.2D_b$) based on three flow variables and two nozzle configurations (BB and BC24). Three grids (coarse '1', medium '2', and fine '3') were investigated

Configuration	Error/GCI	Flow variables used for the GCI study		
		Static temperature $\widetilde{T}_g$	$(H_2O)_v$ molar fraction $\widetilde{X}_w$	Axial velocity $\widetilde{w}_g$
BB	$\varepsilon^{32}_{BB,coarse}$, %	0.00869	0.0847	0.131
	$\varepsilon^{21}_{BB,fine}$, %	0.00969	0.359	0.0101
	$GCI^{32}_{BB,coarse}$, %	0.11	0.57	0.2
	$GCI^{21}_{BB,fine}$, %	0.0979	0.12	0.11
BC24	$\varepsilon^{32}_{BC24,coarse}$, %	0.0319	0.406	0.00444
	$\varepsilon^{21}_{BC24,fine}$, %	0.0152	0.105	0.0252
	$GCI^{32}_{BC24,coarse}$, %	0.21	0.66	0.03748
	$GCI^{21}_{BC24,fine}$, %	0.00364	0.15	0.00598

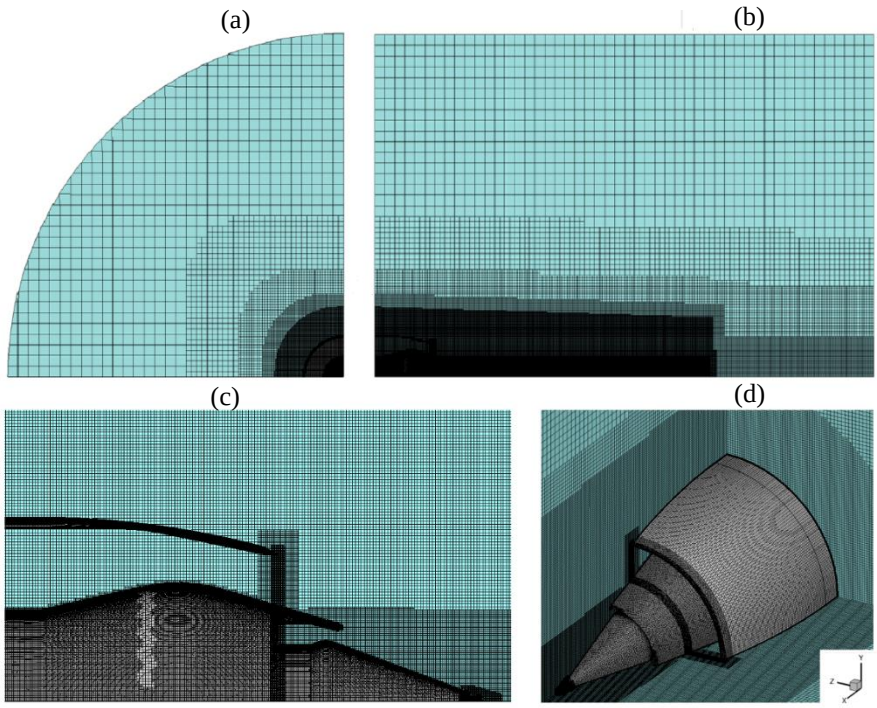

Figure 4: Computational grid for the medium mesh: (a) axial view, (b) lateral view, (c) close-up view of the nozzle exit, (d) isometric view of the engine

Table 4 presents the cell size in each fluid region for the medium mesh. Refinement blocks were used in the engine internal ducts and the near-field ($\leq 10\ m$), where gradients are expected to be relatively high. The cell size in the core internal duct was $\Delta x = 1.5\times10^{-2}$ m, and $\Delta x = 3\times10^{-3}$ m in the bypass internal duct. The mesh in the far field is relatively coarser with cells about $\Delta x = 0.3$ m. The near-wall refinement ensured a maximum y^+ of five, which makes it possible to resolve the boundary layer with wall-law function. As such, the mesh includes a total of 15 prismatic layers orthogonal to bypass duct walls, core duct walls, and engine nacelle. Lastly, a time step $\Delta t = 10^{-3}\ s$ ensured that the maximum Courant number is about unity within the whole computational domain except in the potential core region where the flow speed is equal to core exit velocity $U_c = 460\ m.s^{-1}$ ($M_c = 1$) and the CFL reached a value of about 10.

Table 4: Mesh specifications on boundary conditions for the medium grid '2'

Volume region	Cell size Δx (m)	Number of prismatic layers
Engine nacelle	0.03	15
Bypass internal duct	0.03	15
Core internal duct	0.015	15
Central plug	0.006	15
Engine near-field $\leq 10\ m$	0.0375	-
Engine plume $\leq 100\ m$	0.15	-
Far-field region	0.3	-

3.6 Numerical methods: discretization schemes and coupling strategy

The CFD solver is based on a cell-centered finite-volume approach for unstructured grids [41]. The SIMPLE algorithm was used to solve the flow governing equations. A second-order upwind scheme was used for space discretization, while time integration was achieved with a second-order Euler scheme. For the model of ice-particle growth, a fourth-order Runge-Kutta scheme was used to discretize the Equation (23) of particle size change (more details this discretization can be found in a previous work [14]). The microphysical module was implemented as a user-defined function in the commercial CFD code in Simcenter Star-CCM+ v16.06. The methodology for coupling with the CFD solver is detailed in Figure 5. For instance, the primary flow variables of both gas and dispersed phases are derived at each time step from the CFD solver. The pressure and temperature at each grid point help to compute the thermodynamic variables (P_w, $P^0_{w,liq}$, C_T, and C_ρ), allowing derivation of the local saturation ratio. The residence time (τ_p) of each particle is computed at each time step. Radius of new particles (τ_p=0) is initialized with a monodisperse distribution using an initial radius of $r_{p,0}$. For the following time steps, the evolution of particle radius depends on the local saturation ratios (S_{liq} and S_{ice}) and the current particle radius. A particle-radius table is used to retrieve old particle data (for which the residence time $\tau_p > 0$). Non-saturated particles keep the same radius, while saturated particles grow by water vapour condensation. One should note that ice sublimates from particles when $S_{ice} < 1$ and $r_p > r_{p,0}$. The rates of change for particle mass ($\dot{m}_p$) and size ($\dot{r}_p$) are computed using Equations (22) and (23). At each time step, the particle-radius table is updated and the mass-transfer coupling term $\overline{\omega}_{\mathrm{ice}}$ is computed using Equation (25) and then injected into the CFD solver to correct the water-mass fraction for the following time step.

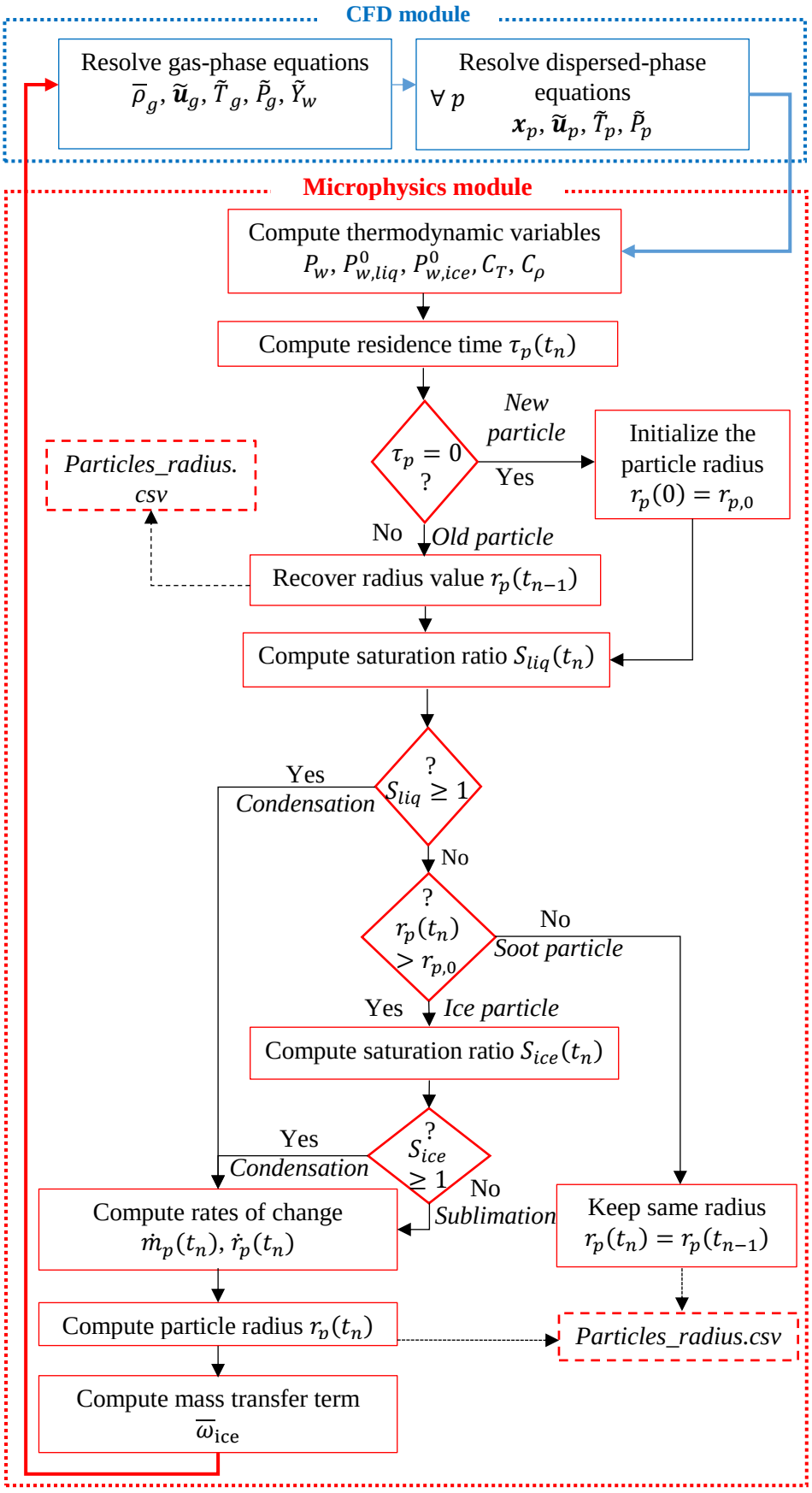

Figure 5: Schematic of the CFD-microphysics coupling for modeling ice-particle growth

4.0 RESULTS ANALYSIS

4.1 Plume dynamic properties

4.1.1 Plume dilution validation

The dilution ratio N defined by Schumann, Schlager [42] was used to characterize the evolution of flow variables (such as temperature and contrail diameter) along the exhaust plume. The dilution ratio based on a passive scalar Z was calculated as follows

$$N = \frac{N_{exit}}{\tilde{Z}} \tag{28}$$

where N_{exit} is the dilution factor at the exhaust section [42] and $\tilde{Z}$ is the ratio of the amount of fluid from the jet region to that from the freestream.[43]. The latter was calculated from

$$\tilde{Z} = \frac{\tilde{Z}_{y,plume} - \tilde{Z}_{i,atm}}{\tilde{Z}_{i,jet} - \tilde{Z}_{i,atm}} \tag{29}$$

where $\tilde{Z}_{y,plume}$ is the passive scalar concentration in the exhaust plume, $\tilde{Z}_{i,atm}$ is the initial atmospheric concentration, and $\tilde{Z}_{i,jet}$ denotes the initial jet concentration. The concentration measurement was taken along the plume centerline.

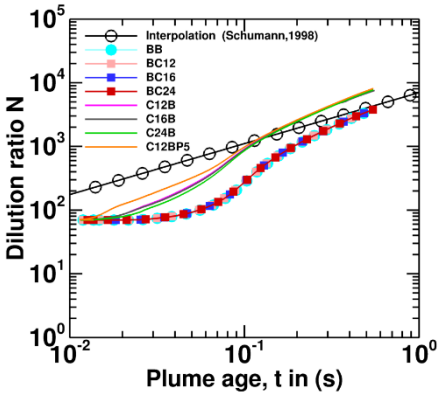

Figure 6: Evolution of the predicted dilution ratio along the engine jet centerline against in-flight interpolated measurements[58]

Figure 6 shows the evolution of the dilution ratio N as function of the plume age for different nozzle configurations (see Table 1): baseline configuration without chevrons (BB), chevron bypass-nozzles (BC12, BC16, BC24), chevron core-nozzles with 0° penetration angle (C12B, C16B, C24B), and with 5° penetration angle (C12BP5). Results are also compared to the bulk mean dilution which are interpolated from a large-set of in-flight measurements (more than 70 plume encounters) with the DLR Falcon research aircraft and the NASA ER-2 aircraft [44]. Overall, the numerical results along the plume centerline showed a good agreement with the in-flight interpolated-data; differences are less than one order of magnitude. One should note that the bulk mean dilution ratio corresponds to the radial average across the plume cross-section at a given distance from the nozzle exit. This explains the relatively higher differences observed especially in early plume between centerline-predicted results and the bulk mean measurements (as also highlighted by Schumann, Ström [44]). Regarding the nozzle configuration effect on the plume dilution ratio, the effect of three nozzle parameters can be discussed: chevron location, chevron number, and the chevron penetration angle. One the one hand, adding chevrons on the core-nozzle clearly showed an enhanced plume dilution ratio (by a factor of 2 to 5) as compared to the baseline nozzle configuration, while no effect was observed on the plume centerline dilution when adding chevrons on the bypass-nozzle. On the other

hand, the number of chevrons did not show a significant effect on the plume dilution ratio for both core and bypass nozzles. One might note a slightly improved plume dilution for the C12B and C16B configurations as compared to chevron core-nozzle C24B. Finally, inclined chevrons on the core-nozzle (C12BP5) improved the plume dilution by a factor about 1.5 as compared to chevron core-nozzles having 0° penetration angle.

4.1.2 Chevron effect on the plume temperature

Figure 7-a presents the static temperature scaled profiles for the 8 studied nozzle configurations along the plume centerline axis while the radial spanwise profiles at $x = 0.1D_b$ and $x = 10D_b$ downstream of the engine exit are presented in Figure 7-b and -c, respectively. Results of plume temperature dilution confirmed previous findings; for instance, adding chevrons on the fan-nozzle did not show any difference as compared to the baseline nozzle without chevrons for both axial and radial profiles. However, the chevron core-nozzle C12B and C16B slightly decreased the static temperature as compared to the baseline nozzle BB and the C24B configuration for $x < 18D_b$ and $r < 0.3r_b$. One should note that all nozzle configurations provide a similar potential core region whose extent is about $L_{pc} = 3D_b$ in plume length (Figure 7-a) and $R_{pc} = 0.15r_b$ in plume radius (Figure 7-b). The core-nozzle with inclined chevrons (C12BP5) provided the lowest plume temperature for $3D_b < x < 20D_b$. The comparison of radial profiles within the potential core region (i.e. at $x = 0.1D_b$ as in Figure 7-b) clearly differentiated the temperature profile of C12BP5 configuration from non-inclined chevron nozzles. At $x = 10D_b$ (Figure 7-c), the axial plume temperature for the C12BP5 nozzle is 15% lower than for the C12B nozzle. Beyond $x = 30D_b$, the plume temperature dilution for all nozzle configurations converged to reach the ambient temperature value.

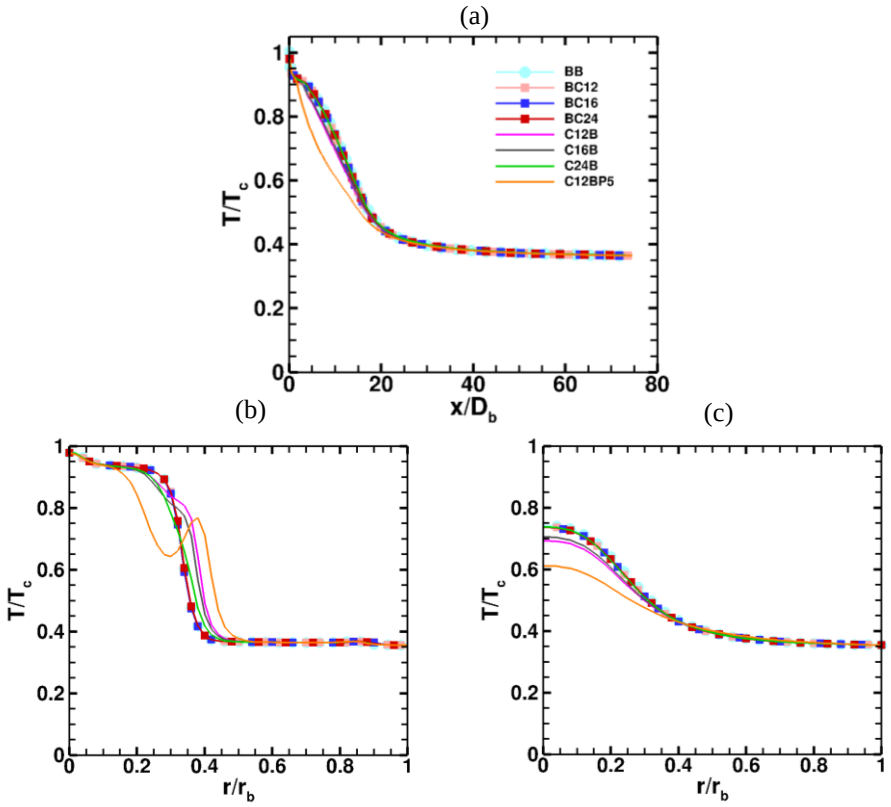

Figure 7: Static temperature profiles along: (a) the plume centerline axis, and (b) radial temperature profiles at $x = 0.1D_b$ (b) and $x = 10D_b$ (c) downstream locations in the near-field of the engine jet

The qualitative comparison of streamwise contours of static temperature for the 8 studied nozzles are presented in Figure 8. The baseline and the three fan-chevron nozzles appear to be very similar (Figure 8-a, -c, and -d). However, when comparing the influence of the location of chevrons on the core versus on the fan (i.e. BC12 and C12B), it seems that the static temperature spread out relatively faster with chevron core-nozzles. Regarding the impact of the chevron penetration angle as illustrated in Figure 8-b, the inner shear layer within the C12BP5 nozzle plume is clearly more spread out as compared to the C12B nozzle, which resulted in a lower temperature at $x = 5D_b$.

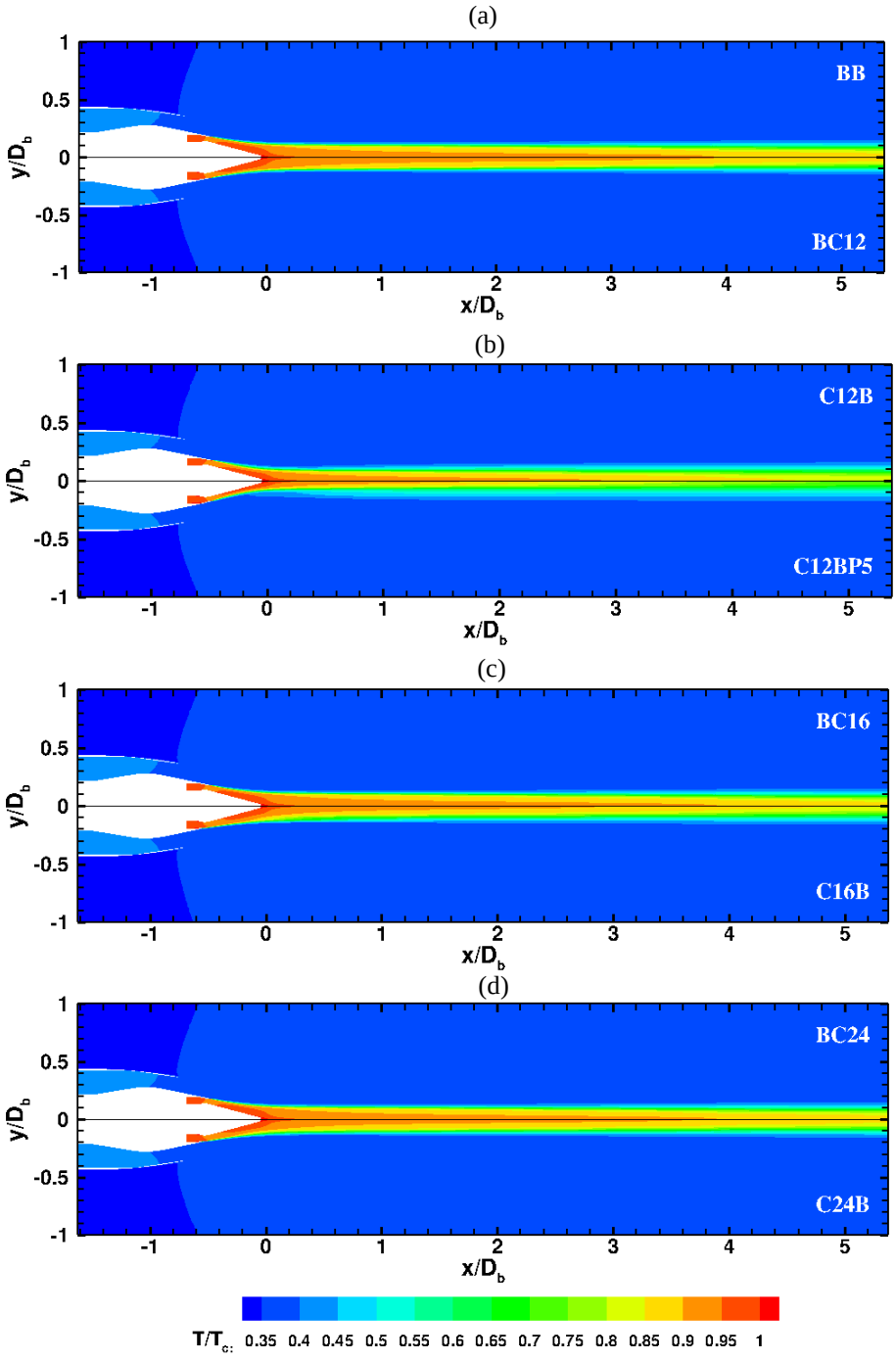

Figure 8: Streamwise contours of static temperature for: (a) BB vs BC12, (b) BC16 vs C16B, (c) C12B vs C12BP5, and (d) BC24 vs C24B

4.1.3 Chevron effect on turbulent-flow characteristics

Figure 9 compares spanwise contours (yz-plane) of turbulent kinetic energy (TKE) for the 8 studied chevron nozzles. The TKE field was scaled by the square of the core jet velocity U_c. For brevity, only one quarter of the spanwise contour is presented for each nozzle configuration. The comparison of TKE were performed at two plume location downstream the engine exhaust: $x = 0.1D_b$ (top row) and $x = 0.75D_b$ (bottom row). One can see that the TKE in the inner/outer shear layers is clearly affected by the presence of the chevron on core/fan nozzles. For instance, the chevrons patterns can be easily discerned on the TKE contours as observed in the form of ripples at $x = 0.1D_b$ (top row). The presence of chevrons on the core nozzle provided a higher TKE as compared to chevron fan-nozzles. The chevron penetration angle seems to further increase the TKE in the inner shear layer (see Figure 9, left column). Moving downstream to $x = 0.75D_b$ (see Figure 9, bottom row), the TKE decrease due to its dissipation for the core-chevron nozzles whereas fan-chevrons and baseline nozzles show a slight increase. As highlighted by Saiyed, Bridges [45], results of plume TKE confirmed that chevrons on the fan nozzle are not as effective as they are on the core nozzle from the plume mixing point of view. In the following section, the effect of chevrons on contrail microphysical properties is assessed.

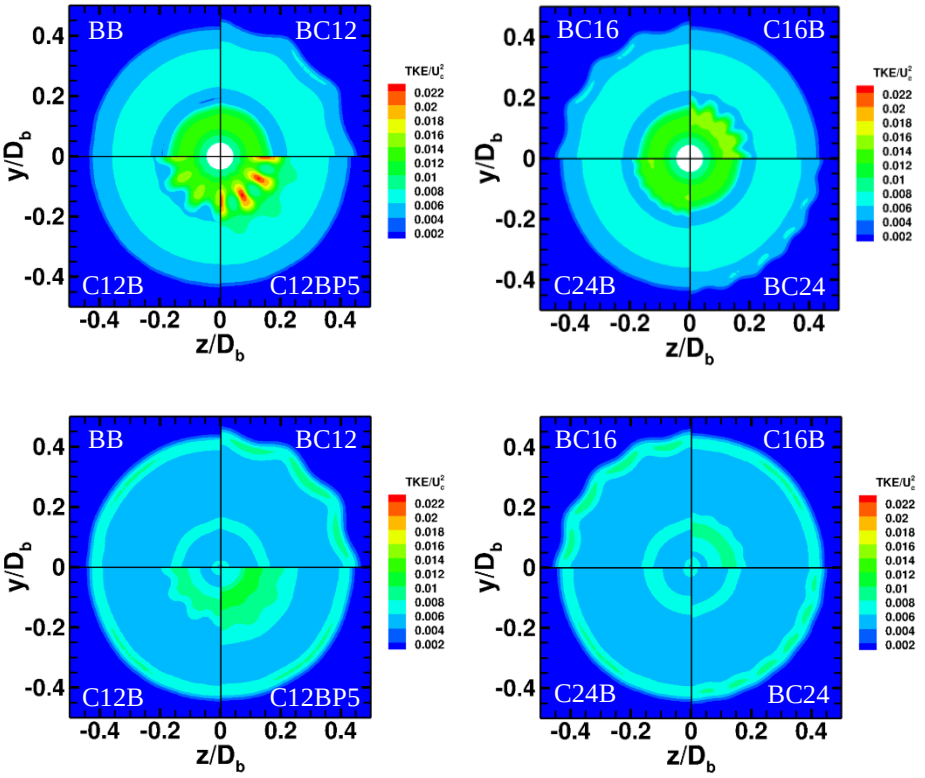

Figure 9: Comparison of ¼-spanwise contours (yz-plane) of turbulent kinetic energy for BB, BC12, C12B, C12BP5 nozzles (left column) and for BC16, C16B, C24B, BC24 nozzles (right column) at two plume locations: $x = 0.1D_b$ (top row) and $x = 0.75D_b$ (bottom row) downstream the engine exhaust

4.2 Jet-contrail microphysical properties

4.2.1 Chevron effect on plume saturation ratio

Figure 10 shows the evolution of the mean saturation ratio of particles with respect to liquid water for the different studied nozzles. The mean liquid saturation ratio $< S_{liq}(x) >$ corresponds to the arithmetic average of particle liquid saturation ratio over the subdomain of length h centered on the position x, defined as [7]

$$< S_{liq}(x) >= \frac{1}{h} \int_{x-h/2}^{x+h/2} S_{liq}\, dx' = \frac{1}{N} \sum_{i=1}^{N} S_{liq,i} \tag{30}$$

where N is the particle number within the considered subdomain and $S_{liq,i}$ is the mean liquid saturation ratio of a given particle i. Close to the engine exhaust ($x \leq 30D_b$), chevron core-nozzles showed a higher liquid saturation ratio than for the baseline nozzle and chevron fan-nozzles. The highest mean saturation ratio was recorded behind the chevron core-nozzle C12BP5 having a 5° penetration angle. Quantitatively, a mean saturation ratio of 0.38 was obtained for the C12BP5 nozzle at $x = 10D_b$ while the other nozzles provided values that are 25% to 50% lower. The threshold value of 1 for ice particle formation was hence reached earlier in the plume for the C12BP5 configuration (i.e. about $x = 25D_b$) as compared to the baseline nozzle and the other chevron nozzles (i.e. about $x = 27D_b$). Beyond $x = 30D_b$, the effect of the penetration angle seems to dissipate in the plume such as a similar saturation profile was observed for all chevron core-nozzles. The maximum value of mean saturation ration $\langle S_{liq}(x) \rangle = 1.55$ was reached at $x = 48D_b$ for the four core-chevron nozzles whereas the maximum value $\langle S_{liq}(x) \rangle = 1.4$ was reached at $x = 41D_b$ for the chevron fan and baseline nozzles. Further downstream, the mean liquid saturation ratio decreased and values of $\langle S_{liq}(x) \rangle = 1.45$ and $\langle S_{liq}(x) \rangle = 1.27$ were reached at the end of the computational domain for core chevron nozzles and fan chevron/baseline nozzles, respectively. The latter decrease in mean saturation ratio is mainly due to two concurrent mechanisms that control the microphysical processes in near-field contrails [7]: 1) the turbulent mixing between exhaust and ambient air which cools and dilutes the jet fluid, and 2) the vapor depletion that decreases the amount of vapor available for condensation as this is transformed into ice.

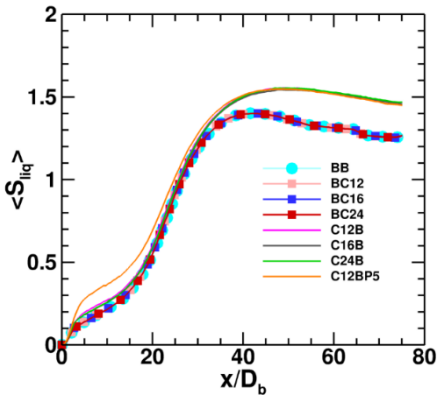

Figure 10: Evolution of mean saturation ratio of particles along the jet plume

4.2.2 Chevron effect on ice particle number and radius

Figure 11-a and -b show the evolutions along the plume jet of the mean particle radius and the ice particles number (expressed), respectively. It should be noted that the number of ice particles (or saturated particle) is expressed by an emission index, EI (#/kg-fuel) that is scaled by the fuel flow rate at cruise regime (20% of the maximum rated thrust) $\dot{m}_{fuel} = 0.32$ kg/s, as defined by Unterstrasser [46]. While the mean particle radius $\langle r_p(x) \rangle$ corresponds to the arithmetic average of particle radii over the subdomain of length h centered on the position y, defined as [7]

$$\langle r_p(x) \rangle = \frac{1}{h} \int_{x-h/2}^{x+h/2} r_p \, dx' = \frac{1}{N} \sum_{i=1}^{N} r_{p,i} \tag{31}$$

where N is the particle number within the considered subdomain and $r_{p,i}$ is the radius of a given particle i. The mean particle radius is initially constant (GMD = 11.64 nm) at the engine exhaust and starts growing around $x = 5D_b$. As the particle radii depend on the rate of water condensation along the exhaust plume which, in turn, is fully determined by the local saturation ratio, the differences highlighted in Figure 10 (above) confirmed the results of mean particle radius in Figure 11-a. For instance, at 0.5 s of the plume age ($x = 72D_b$), the chevron core-nozzles led to a mean ice particle radius (about 0.46µm) that is 25% larger than for baseline and chevron fan-nozzles (about 0.37µm). The latter values of mean particle radius are in the good range of 350 to 700 nm, as confirmed by several numerical studies from the literature [6, 19]. The results of ice particle number in Figure 11-b showed that the production of ice particles soared up to $EI_{iceno} = 6.7 \cdot 10^{13}$ #/kg-fuel at $x = 35D_b$ then inched up to $EI_{iceno} = 7.5 \cdot 10^{13}$ #/kg-fuel at the end of the computational domain. The early steep increase of EI_{iceno} may be due to the saturation of liquid water as noticed by [8, 47], that leads to a rapid formation of ice particles. Even though a quite similar profile of ice particle number was observed for the different nozzle configurations, larger ice particles are obtained in the plumes of chevron core-nozzles (see Figure 11-a).

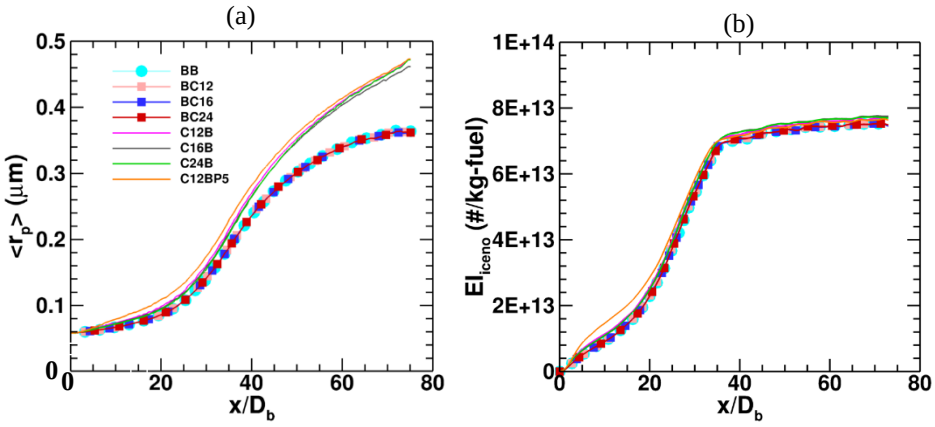

Figure 11: Evolution of the mean particle radius (a) and the emission index of ice particle number (b) along the jet plume

4.2.3 Chevron effect on the optical depth

Lastly, the optical depth τ of the jet contrail was assessed for the different studied nozzle configuration. This parameter measures the attenuation of radiation passing through clouds and is often reported at a wavelength in the visible part of the radiation spectrum [48]. The optical depth τ was hence evaluated in a uniform grid

$$\tau(x,y,z) = \sum_{i=1}^{N_{com,g}} \pi r_p^2 Q_{ext} \frac{N_g}{\Delta V} \tag{32}$$

where $N_{com,g}$ denotes the number of computational particles in the grid cell, N_g the total number of physical particles in the grid cell whose volume is $\Delta V = \Delta x \times \Delta y \times \Delta z$. Equation (33) approximates the Mie extinction efficiency Q_{ext} at a given wavelength λ_w, such as the refractive index for ice of $\mu_r = 1.31$ and the wavelength of visible light is considered as $\lambda_w = 0.55$ µm.

$$Q_{ext} = 2 - \frac{4}{e}\left[\sin(e) - \frac{1-\cos(e)}{e}\right] \tag{33}$$

$$e = \frac{4\pi r_p(\mu_r - 1)}{\lambda_w} \tag{34}$$

The local optical depth τ is then integrated across the plume cross-section to get the mean optical depth along the plume axial direction $< \tau(x) >$. Figure 12 gives the evolution of the mean optical depth of contrails generated behind the eight studied nozzles. The results showed that chevron core-nozzles leads to a contrail having a higher optical depth (factor of 2) as compared to both chevron fan and baseline nozzles. This confirms the conclusions highlighted above regarding the effect of chevron core nozzle in improving the plume dilution, decreasing the plume temperature, increasing the plume saturation ratio, and thus leading to larger ice particles in the associated jet-contrails.

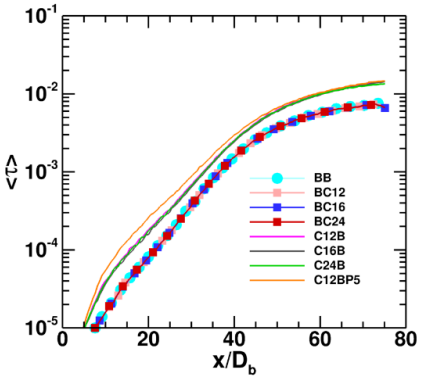

Figure 12: Evolution of optical depth of the plume behind the jet engine

5.0 CONCLUSION

This work aimed at studying the effect of chevron nozzles parameters on the near-field plume properties from a realistic LEAP-1A turbofan engine at cruise flight conditions. As such, 3-D unsteady Reynolds-Averaged Navier-Stokes simulations with an Eulerian-Lagrangian approach were carried out and a CFD-microphysics coupling strategy was proposed to model the 3-D dynamic and microphysical transformations of jet-contrails. A total of 8 nozzles configurations were investigated to cover the effect of chevrons parameters (chevron position, number, and penetration angle): a baseline configuration without chevrons (BB), bypass-nozzles with 12, 16, and 24 chevrons (BC12, BC16, and BC24, respectively), chevron core-nozzles with 0° penetration angle (C12B, C16B, C24B), and with 5° penetration angle (C12BP5). Model validations were performed on the predicted of plume dilution ratios for the different nozzle configurations. The comparison of numerical prediction showed a good agreement with the available in-flight measurements in early plume. Regarding the chevron effect on the early plume properties, results of chevron fan-nozzles showed no effect on the plume dilution, temperature,

saturation ratio, particle radius, or the optical depth. Whereas the chevron core-nozzles enhanced the plume mixing and dilution (by a factor of 2 to 5) as compared to the baseline nozzle configuration. This helped to lower the plume temperature, favor the water condensation and consequently led to a 25% larger ice particles in the jet-contrail as compared to the baseline and chevron fan-nozzles. Changing the number of chevrons did not show any significant effect on the plume dilution ratio for both core and fan nozzles, while the use of inclined chevrons on the core-nozzle with 5° penetration angle helped to locally improve the plume dilution by a factor about 1.5 as compared to the case of chevrons with 0° penetration angle. However, the effect of the penetration angle seems to dissipate quickly beyond the plume position $x = 30D_b$ and similar plume properties were observed for all chevron core-nozzles.

Overall, the comprehensive analysis performed shows that core-chevron nozzle leads to higher kinetic turbulent energy, higher liquid saturation ratio, larger ice particles and thicker contrails than fan-chevron and baseline nozzles. The proposed model can be hence used in future studies to characterize the impact of tabs or lobed nozzle-exit parameters on the optical and microphysical properties of near-field contrails. Research perspectives to be explored next involve the interactions of soot and sulfur species in the early plume mainly focusing on chevron core-nozzles. The latter requires the implementation of a gas-phase chemistry and detailed microphysics of volatile and semi-volatile particles.

ACKNOWLEDGMENTS

This research was enabled in part by support provided by Calcul Québec (calculquebec.ca) and the Digital Research Alliance of Canada (alliancecan.ca). The authors would also like to acknowledge the financial support of Safran Aircraft Engine for this work. This work is part of the Safran Industrial Research Chair on the Development of Sustainable Aero-Propulsion Systems at ÉTS.

REFERENCES

[1] Lee, D.S., et al., "The contribution of global aviation to anthropogenic climate forcing for 2000 to 2018," *Atmospheric Environment*. vol. 244, no.: pp. 117834, 2020

[2] Lee, D.S., et al., "Transport impacts on atmosphere and climate: Aviation," *Atmospheric Environment*. vol. 44, no. 37: pp. 4678-4734, 2010

[3] Kärcher, B., "The importance of contrail ice formation for mitigating the climate impact of aviation," *Journal of Geophysical Research: Atmospheres*. vol. 121, no. 7: pp. 3497-3505, 2016

[4] Schumann, U. and A. Heymsfield, "On the Life Cycle of Individual Contrails and Contrail Cirrus," *Meteorological Monographs*. vol. 58, no.: pp. 3.1-3.24, 2017

[5] Karcher, B., et al., "The microphysical pathway to contrail formation," *Journal of Geophysical Research: Atmospheres*. vol. 120, no. 15: pp. 7893-927, 2015

[6] Vancassel, X., P. Mirabel, and F. Garnier, "Numerical simulation of aerosols in an aircraft wake using a 3D LES solver and a detailed microphysical model," *International Journal of Sustainable Aviation*. vol. 1, no. 2: pp. 139-159, 2014

[7] Paoli, R., et al., "Effects of jet/vortex interaction on contrail formation in supersaturated conditions," *Physics of Fluids*. vol. 25, no. 5: pp. 053305, 2013

[8] Lewellen, D.C., "A Large-Eddy Simulation Study of Contrail Ice Number Formation," *Journal of the Atmospheric Sciences*. vol. 77, no. 7: pp. 2585-2604, 2020

[9] Khou, J.C., et al., "CFD simulation of contrail formation in the near field of a commercial aircraft: effect of fuel sulfur content," *Meteorologische Zeitschrift*. vol. 26, no. 6, 2016

[10] Zaman, K.B.M.Q., J.E. Bridges, and D.L. Huff, "Evolution from 'Tabs' to 'Chevron Technology' - A Review," *International Journal of Aeroacoustics*. vol. 10, no. 5-6: pp. 685-709, 2011

[11] Massey, S., et al., "Computational Analysis of a Chevron Nozzle Uniquely Tailored for Propulsion Airframe Aeroacoustics." in *27th AIAA Aeroacoustics Conference*, Cambridge, Massachusetts, 2006
[12] Callender, B., E.J. Gutmark, and S. Martens, "Flow field characterization of coaxial conical and serrated (chevron) nozzles," *Experiments in fluids*. vol. 48, no. 4: pp. 637-649, 2010
[13] Tide, P.S. and K. Srinivasan, "Effect of chevron count and penetration on the acoustic characteristics of chevron nozzles," *Applied Acoustics*. vol. 71, no. 3: pp. 201-220, 2010
[14] Cantin, S., et al., "Eulerian–Lagrangian CFD-microphysics modeling of a near-field contrail from a realistic turbofan," *International Journal of Engine Research*. vol. 23, no. 4: pp. 661-677, 2021
[15] Kärcher, B., "Physicochemistry of aircraft-generated liquid aerosols, soot, and ice particles: 1. Model description," *Journal of Geophysical Research: Atmospheres*. vol. 103, no. D14: pp. 17111-17128, 1998
[16] Popovicheva, O.B., et al., "Aircraft engine soot as contrail nuclei," *Geophysical Research Letters*. vol. 31, no. 11: pp. n/a-n/a, 2004
[17] CD-Adapco, "STAR-CCM+ Documentation Version 16.06.008." 2021.
[18] Kärcher, B., "Transport of exhaust products in the near trail of a jet engine under atmospheric conditions," *Journal of Geophysical Research: Atmospheres*. vol. 99, no. D7: pp. 14509-14517, 1994
[19] Khou, J.C., et al., "Spatial Simulation of Contrail Formation in Near-Field of Commercial Aircraft," *Journal of Aircraft*. vol. 52, no. 6, 2015
[20] Jones, W.P. and B.E. Launder, "The prediction of laminarization with a two-equation model of turbulence," *International Journal of Heat and Mass Transfer*. vol. 15, no. 2: pp. 301-314, 1972
[21] Shaheed, R., A. Mohammadian, and H. Kheirkhah Gildeh, "A comparison of standard k–ε and realizable k–ε turbulence models in curved and confluent channels," *Environmental Fluid Mechanics*. vol. 19, no. 2: pp. 543-568, 2019
[22] Thies, A.T. and C.K.W. Tam, "Computation of turbulent axisymmetric and nonaxisymmetric jet flows using the K-epsilon model," *AIAA Journal*. vol. 34, no. 2: pp. 309-316, 1996
[23] Schröder, F., et al., "In situ studies on volatile jet exhaust particle emissions: Impact of fuel sulfur content and environmental conditions on nuclei mode aerosols," *Journal of Geophysical Research: Atmospheres*. vol. 105, no. D15: pp. 19941-19954, 2000
[24] Schröder, F., et al., "On the transition of contrails into cirrus clouds," *Journal of the Atmospheric Sciences*. vol. 57, no. 4: pp. 464-80, 2000
[25] Paoli, R., J. Hélie, and T. Poinsot, "Contrail formation in aircraft wakes," *Journal of Fluid Mechanics*. vol. 502, no.: pp. 361-373, 2004
[26] Schumann, U., "On Conditions for Contrail Formation from Aircraft Exhausts." vol. 5, no.: pp. 4-23, 1996
[27] Jensen, E.J., et al., "Environmental conditions required for contrail formation and persistence," *Journal of Geophysical Research*. vol. 103, no. D4: pp. 3929-36, 1998
[28] Murphy, D.M. and T. Koop, "Review of the vapour pressures of ice and supercooled water for atmospheric applications," *Quarterly Journal of the Royal Meteorological Society*. vol. 131, no. 608: pp. 1539-1565, 2005
[29] Koehler, K.A., et al., "Cloud condensation nuclei and ice nucleation activity of hydrophobic and hydrophilic soot particles," *Physical Chemistry Chemical Physics*. vol. 11, no. 36: pp. 7906-7920, 2009
[30] Hartmann, S., et al., "Homogeneous and heterogeneous ice nucleation at LACIS: Operating principle and theoretical studies," *Atmospheric Chemistry and Physics*. vol. 11, no. 4: pp. 1753-1767, 2011
[31] Fukuta, N. and L.A. Walter, "Kinetics of Hydrometeor Growth from a Vapor-Spherical Model," *Journal of the Atmospheric Sciences*. vol. 27, no. 8: pp. 1160-1172, 1970
[32] Timmerman, B.H., et al., "Large-scale time-resolved digital particle image velocimetry (TR-DPIV) for measurement of high subsonic hot coaxial jet

exhaust of a gas turbine engine," *Measurement Science and Technology*. vol. 20, no. 7: pp. 074002, 2009

[33] Munday, D., et al., "Supersonic Jet Noise Reduction Technologies for Gas Turbine Engines," *Journal of Engineering for Gas Turbines and Power*. vol. 133, no. 10, 2011

[34] Callender, B., E. Gutmark, and S. Martens, "Near-Field Investigation of Chevron Nozzle Mechanisms," *AIAA Journal*. vol. 46, no. 1: pp. 36-45, 2008

[35] Callender, B., E. Gutmark, and S. Martens, "Far-Field Acoustic Investigation into Chevron Nozzle Mechanisms and Trends," *AIAA Journal*. vol. 43, no. 1: pp. 87-95, 2005

[36] ICAO, *Aircraft Engine Emissions Databank*. 2021.

[37] EASA, *Type-certificate data sheet for LEAP-1A & LEAP-1C series engines*, C.I. SA, Editor. 2016: 2, boulevard du Général Martial Valin, F-75724 Paris Cedex 15, France.

[38] van Holsteijn, M.R., A. Gangoli Rao, and F. Yin, "Operating Characteristics of an Electrically Assisted Turbofan Engine." in *ASME Turbo Expo 2020: Turbomachinery Technical Conference and Exposition*, 2020

[39] Agarwal, A., et al., "SCOPE11 Method for Estimating Aircraft Black Carbon Mass and Particle Number Emissions," *Environ. Sci. Technol.* vol. 53, no. 3: pp. 1364–1373, 2019

[40] Celik, I.B., et al., "Procedure for Estimation and Reporting of Uncertainty Due to Discretization in CFD Applications," *Journal of Fluids Engineering*. vol. 130, no. 7: pp. 078001-078001-4, 2008

[41] Patankar, S.V. and D.B. Spalding, "A calculation procedure for heat, mass and momentum transfer in three-dimensional parabolic flows," *International Journal of Heat and Mass Transfer*. vol. 15, no. 10: pp. 1787-1806, 1972

[42] Schumann, U., et al., "Dilution of aircraft exhaust plumes at cruise altitudes," *Atmospheric Environment*. vol. 32, no. 18: pp. 3097-3103, 1998

[43] Garnier, F., et al., "Engine emission alteration in the near field of an aircraft," *Atmospheric Environment*. vol. 31, no. 12: pp. 1767-1781, 1997

[44] Schumann, U., et al., "In situ observations of particles in jet aircraft exhausts and contrails for different sulfur-containing fuels," *Journal of Geophysical Research: Atmospheres*. vol. 101, no. D3: pp. 6853-6869, 1996

[45] Saiyed, N., J. Bridges, and K. Mikkelsen, "Acoustics and thrust of separate-flow exhaust nozzles with mixing devices for high-bypass-ratio engines." in *21st AIAA Aeroacoustics Conference*, Lahaina, HI,U.S.A., 2000

[46] Unterstrasser, S., "Properties of young contrails – a parametrisation based on large-eddy simulations," *Atmospheric Chemistry and Physics*. vol. 16, no. 4: pp. 2059-2082, 2016

[47] Bier, A., S. Unterstrasser, and X. Vancassel, "Box model trajectory studies of contrail formation using a particle-based cloud microphysics scheme," *Atmospheric Chemistry and Physics*. vol. 22, no. 2: pp. 823-845, 2021

[48] Kärcher, B., "Formation and radiative forcing of contrail cirrus," *Nature communications*. vol. 9, no. 1: pp. 1824, 2018